Check for updates

Chemistry
Europe
European Chemical
Societies Publishing

Towards stable and high-capacity anode materials for sodium-ion batteries by embedding of Sb/Sn nanoparticles into electrospun mesoporous carbon fibers

Tian Liu[1,+] | **Runyu Yan[2,+]** | **Elinor Josef[2]** | **Haijian Huang[1]** | **Long Pan[1]** | **Markus Niederberger[1]** | **Martin Oschatz[2,3]**

[1] Laboratory for Multifunctional Materials, Department of Materials, ETH Zürich, Vladimir-Prelog-Weg 5, Zürich 8093, Switzerland

[2] Department of Colloid Chemistry, Max Planck Institute of Colloids and Interfaces, Am Mühlenberg 1, Potsdam 14476, Germany

[3] Institute for Technical Chemistry and Environmental Chemistry, Center for Energy and Environmental Chemistry Jena (CEEC Jena), Friedrich-Schiller-University Jena, Philosophenweg 7a, Jena 07743, Germany

Correspondence
Martin Oschatz, Department of Colloid Chemistry, Max Planck Institute of Colloids and Interfaces, Am Mühlenberg 1, 14476 Potsdam, Germany.
Email: martin.oschatz@uni-jena.de
Markus Niederberger, Laboratory for Multifunctional Materials, Department of Materials, ETH Zürich, Vladimir-Prelog-Weg 5, Zürich, 8093, Switzerland.
Email: markus.niederberger@mat.ethz.ch

[+]T.L. and R.Y. contributed equally

Abstract
Antimony and tin are promising anode materials for sodium-ion batteries due to their high theoretical sodium storage capacities. However, significant volume change during cycling limits their long-term stability and rate performance. Composite engineering can minimize this problem. A versatile method for the synthesis of Sb nanoparticles inside the mesopores of carbon fibers prepared through electrospinning and subsequent carbothermal reduction is presented in this work. The mesopore architecture can host up to 61 wt% of Sb nanoparticles and buffer the volume changes during cycling. Smaller pores in the carbon provide the pathways for reversible insertion/extraction of sodium. This binder-free material provides high rate capability and a long-term cycling performance when used as an anode in half-cells. When cycled at 0.5 A g^{-1}, the composite shows an initial capacity of 520 mA h g^{-1} with 507 mA h g^{-1} remaining after 500 cycles. Even at a high current density of 20 A g^{-1}, a capacity of 197 mA h g^{-1} is still achieved. Sn nanoparticles can be embedded in the mesopores of the carbon fibers by a similar method. These Sn-based anodes also show remarkable electrochemical performance, indicating that this approach represents a generally applicable strategy for synthesizing advanced battery anodes.

KEYWORDS
anodes, electrospinning, mesoporous carbon fibers, metal nanoparticles, sodium-ion batteries

1 | INTRODUCTION

Lithium-ion batteries (LIBs) are prime candidates for energy storage due to their high working voltage, high energy density, and stable cycling performance.[1] With the sharply increasing demand for LIBs in portable electronics, electric vehicles, and power grids, concerns about the available resources and price of lithium arise.[2] Sodium-ion batteries (SIBs) are considered promising alternatives to LIBs.[3] Due to the abundant resources of sodium, SIBs have great potential to fulfill the enormous future demand, especially for large-scale electrochemical energy storage.

Although graphite is the established material in commercial LIBs, a suitable compound for sodium storage in SIB anodes has still not been found. Carbonaceous materials (most often hard-carbon) and their composites,[4] metal oxides/sulfides,[4b,5] and metals/alloys[6] have been studied. Among them, Sb and Sn are particularly attractive due to their low working potentials and high theoretical capacities of 660 mA h g^{-1} and 847 mA h g^{-1}, respectively.[7] However, one major drawback is that both elements experience large volume expansions (up to 390 % for Sb[8] and up to 420 % for Sn[9]) during sodiation/desodiation. Such enormous volume change during cycling usually leads to the pulverization of the electrodes, often resulting in the loss of electrical contact between the particles and the current collector. Furthermore, due to the continuous formation of new solid electrolyte interphase (SEI) on the exposed surfaces, the high initial capacities of Sb/Sn are usually accompanied by low Coulombic efficiencies and severe capacity fading during cycling.[10]

Up to now, several strategies have been proposed to address these problems of bulk metallic anode materials and the corresponding extensive volume changes during cycling. Among them, one prevalent strategy is to reduce the size of the particles to alleviate higher strain and retard pulverization. For example, Wang et al. found that the alkali metal storage properties of Sn/SnO$_x$ core−shell spheres are strongly depending on their size. Small particles of 30 and 45 nm significantly outperformed larger sub-micro-sized (100–500 nm) and micro-sized (0.3–10 μm) particles.[11] The smooth surfaces of micro-sized particles coarsened during cycling, lowering their adhesion to the conductive carbon black matrix which was added by physical mixing. The detachment of active materials and conductive matrix leads to the deterioration of electronic contact between individual particles and by that capacity fading. Even though downscaling of the sizes of the metallic alloy anode particles is an effective way to mitigate the volume incongruity, the cyclability remains limited by particle aggregation.[12] The latter is accelerated by the significantly higher surface energy, lower melting point, and changed redox potentials of nanoparticles in comparison to the corresponding bulk metal. These differences all have to be considered when downscaling of particle sizes is considered as the method to minimize pulverization of electrode materials.

Following a principle that is established in heterogeneous catalysis and other electrochemical energy storage devices such as lithium-sulfur batteries for a long time, nanostructured carbonaceous materials have been widely applied to disperse the metallic alloy anode nanoparticles in a porous matrix to prevent their agglomeration, buffer the volume change, and enhance the ion transport during cycling. From a fundamental perspective, such "carbon-supported" composite electrode materials can potentially contribute to the solution of the so-called "Ragone dilemma" by decoupling storage and transport of electrons and metal (ions).[13] For instance, advanced architectures like self-wrapped Sb/C nanocomposites,[14] Sn@sheet-like nitrogen-doped carbon foams[15] and graphene/Sn-nanopillars[16] show impressive rate capability and long cyclability in SIBs. Among the different materials, electrospun carbon fibers are particularly attractive, because the one-dimensional morphology offers a defined texture in combination with high electronic conductivity without contact resistance between particles as in powder materials.[17] Electrospinning is a scalable method and allows to adjust the textural properties of the electrode materials such as fiber thickness and density. Several studies demonstrated that metal and metal alloy nanoparticles such as Sb,[14] Sn,[18] and SnSb[19] can be encapsulated into polymer fibers during electrospinning which can then be carbonized. This approach enables the synthesis of promising materials for stable sodium-ion battery anodes with high capacity and it can be expected that further optimization of the structural design, e.g., by introducing additional porosity, could further enhance the rate capability and cycling stability of the metal and metal alloy/carbon composite anodes.[20] However, a more profound understanding of the interplay between different structural parameters of the electrode materials and their electrochemical properties is still necessary to make the maximum possible use of this concept towards advanced SIBs anodes.

A method for the preparation of one-dimensional porous carbon fibers with encapsulated Sb (Sb-PCF) or Sn nanoparticles (Sn-PCF) by electrospinning, followed by carbothermal processing is reported here. The unique architecture and the bimodal porosity of the composite come with several advantages when applied as SIBs anode as shown by comparison to suitable reference materials. The mesoporous carbon fiber matrix prevents the nanoparticles from aggregation. The micropores present in the fibers provide pathways for ion transport. The mesopores encapsulating the Sb and the Sn nanoparticles offer space to buffer the volume change of the metals. In consequence, the two composites exhibit high specific capacities of 507 mA h g^{-1} and 428 mA h g^{-1} after 500 cycles at 0.5 A g^{-1}, respectively. Good rate capability and long cyclability over 500 cycles are achieved.

2 | RESULTS AND DISCUSSION

Scheme 1 illustrates the preparation process of the Sb-PCF composite. First, an electrospinning process was employed using a precursor mixture containing Sb$_2$O$_3$ nanoparticles, polyacrylonitrile (PAN), and
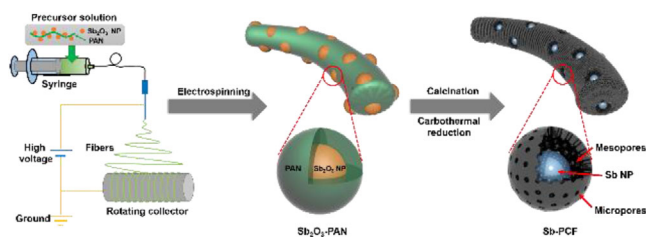
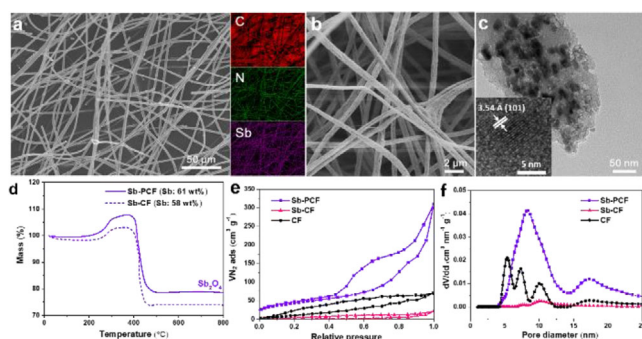**SCHEME 1** Synthesis process for the Sb-PCF composite

FIGURE 1 (A, B) SEM images of Sb-PCF at different magnifications. The inset in (A) shows the corresponding elemental mapping SEM-EDX (C, N, and Sb); (C) TEM and HRTEM images (inset) of the Sb-PCF; (D) TGA of Sb-PCF and Sb-CF in air; (E) nitrogen physisorption (at −196°C) isotherms with (F) corresponding QSDFT pore size distribution of Sb-PCF, Sb-CF, and CF

dimethylformamide (DMF). The electrospun fibers were then heated under inert atmosphere to form the Sb-PCF composites. During annealing, PAN transformed into nitrogen-doped carbon, and the Sb_2O_3 nanoparticles were reduced into metallic Sb nanoparticles, which are embedded into the carbon framework.[23] This process has two effects on the microstructure of the composite. On the one hand, small pores grow in the fiber because of the polymer decomposition and carbon oxide gases produced. On the other hand, mesopores with embedded Sb nanoparticles are formed during the reduction of the Sb_2O_3 nanoparticles. As reference samples, carbon fibers (CF) and Sb encapsulated carbon fibers (Sb-CF) were synthesized with an electrospinning method reported by Zhu et al.[22]

As shown in the transmission electron microscopy (TEM) overview image (Supporting Information Figure S1A), the particle size of the Sb_2O_3 nanoparticles is around 5 nm. The X-ray powder diffraction (XRD) pattern shows that the diffraction signals agree well with the cubic phase of Sb_2O_3 (JCPDS No. 5–534) (Supporting Information Figure S1C).[24] The morphology of Sb-PCF at two different magnifications is depicted in the scanning electron microscopy (SEM) images (Figure 1A and B). The fibers exhibit rough surfaces, have a uniform diameter of around 600 nm, and are present as interconnected

networks. The elemental mapping SEM energy dispersive X-Ray (EDX) (insets in Figure 1A) demonstrates that C, N, and Sb are uniformly dispersed in the carbon fiber matrix. Additionally, the XRD pattern of Sb-PCF confirms the presence of crystalline Sb nanoparticles with a hexagonal crystal structure (JCPDS No. 35–0732) (Figure S1D, supporting information).[25] TEM was further used to analyze the micro- and nanostructure of the Sb-PCF composite, which reveals the distribution and encapsulation of the Sb nanoparticles in the carbon fibers. The high-resolution transmission electron microscopy (HRTEM) image (inset, Figure 1C) shows that the crystal size of the Sb nanoparticles is approximately 3–4 nm. The measured d-spacing of the selected nanoparticle is 0.354 nm and corresponds to the (111) plane of Sb. The Sb/carbon ratio was evaluated by thermogravimetric analysis (TGA) under air (Figure 1D), based on the weight loss resulting from carbon combustion and the weight gain due to Sb_2O_4 formation. The content of Sb in the composite was calculated to be 61 wt% assuming that Sb_2O_4 is the final product of the TGA measurement.[25a,26] For comparison, $SbCl_3$ was also used as the precursor to fabricate Sb impregnated carbon fibers (Sb-CF) according to a previous study.[22] TGA analysis shows that the Sb-CF has a comparable Sb content of 58 wt%. N_2 physisorption experiments show that Sb-PCF presents a typical Type IV isotherm with a continuous slope above the relative pressure of 0.2 and a hysteresis loop in the relative pressure range between 0.4 and 0.9, which indicates the existence of mesopores (Figure 1E). The pronounced N_2 uptake in the relative pressure range of below 0.2 indicates the presence of additional smaller micropores. In comparison, Sb-CF and CF show isotherms with lower N_2 uptake, pointing toward a rather dense structure with only a few pores of random sizes that are accessible for nitrogen.[17,27] Pore size distribution analysis using the quenched solid density functional theory (QSDFT) confirms the presence of mesopores with diameters in the range from 5 to 20 nm in the Sb-PCF composite (Figure 1F). Sb-PCF has the highest specific surface area (SSA) of 155 m^2 g^{-1} and total pore volume (TPV) of 0.33 cm^3 g^{-1} among all samples. Sb-CF (2.5 m^2 g^{-1} of SSA and 0.02 cm^3 g^{-1} of TPV) and CF (51 m^2 g^{-1} of SSA and 0.09 cm^3 g^{-1} of TPV) have significantly lower porosity (Table S1, supporting information). The pore structures of Sb-PCF, Sb-CF, and CF were also characterized by TEM. Sb-PCF shows a coarse morphology with a loose feature, which indicates the significant mesopore content (Supporting Information Figure S2A–C). In contrast, Sb-CF (Supporting Information Figure S2D–F) exhibits a rather dense structure while CF presents a smooth surface and dense morphology (Supporting Information Figure S2G–I), which is in accordance with the N_2 physisorption measurements.
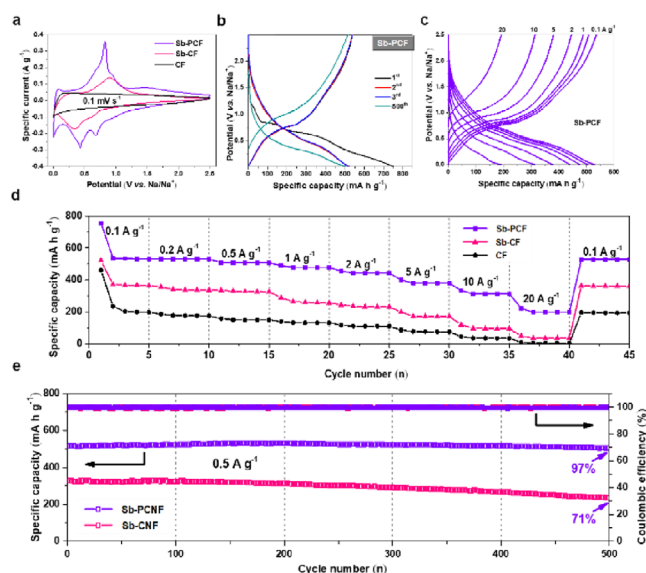
4 of 8 **Electrochemical Science Advances** Full article
doi.org/10.1002/elsa.202100010

Chemistry
Europe
European Chemical
Societies Publishing

FIGURE 2 (A) Cyclic voltammograms of the Sb-PCF, Sb-CF, and CF composites between 0 and 2.5 V at a scanning rate of 0.1 mV s^{-1}; (B) galvanostatic charge-discharge profiles of Sb-PCF for the first three and the 500th cycle at a current density of 0.1 A g^{-1}; (C) galvanostatic charge-discharge profiles and (d) rate performance of Sb-PCF cycled at various current densities from 0.1 A g^{-1} to 20 A g^{-1}; (E) cycling performance of Sb-PCF and Sb-CF at a cycling rate of 0.5 A g^{-1}

The sodium storage properties of Sb-PCF, Sb-CF, and CF were studied in half-cell configurations using sodium metal as the reference and counter electrode. The cyclic voltammetry (CV) measurements of Sb-PCF, Sb-CF, and CF were performed at a scan rate of 0.1 mV s^{-1} within the voltage range of 0–2.5 V (vs. Na$^+$/Na) (Figure 2A). For Sb-PCF, the two redox peaks observed at 0–0.1 V can be ascribed to the insertion and extraction of sodium in the interlayer of the graphitic microcrystallites.[28] The subsequent reduction peaks at around 0.43 V and 0.68 V can be attributed to different sodiation steps of Sb, producing Na$_x$Sb and Na$_3$Sb.[29] The oxidation peaks at 0.83 V and 0.93 V are caused by the corresponding two-step desodiation process of Na$_3$Sb and Na$_x$Sb.[25a] The broad oxidation peak centered around 1.4 V might be a result of the reversible binding between sodium ions and the nitrogen-containing functional surface groups which can act as high energy stabilization sites for sodium as proposed previously.[30] For comparison, the CV curve of Sb-CF shows the sodiation peaks corresponding to the formation of Na$_x$Sb and Na$_3$Sb at 0.61 V and 0.34 V, respectively. The merged peak around 0.9 V is attributed to desodiation of Na$_3$Sb and Na$_x$Sb.[25a,29] Compared with Sb-PCF, the much smaller volume of nanopores of Sb-CF leads to sluggish ion transport. This causes larger polarization in Sb-CF, giving rise to the larger overpotentials for the reaction.[31] The very broad reduction peak in the CV curve of CF

is attributed to the intercalation of sodium ions between the graphene layers in the carbon fibers.[32] Galvanostatic charge-discharge profiles of Sb-PCF for the first three and the 500th cycle at a current density of 0.1 A g^{-1} (Figure 2B) show that the initial discharge and charge capacities of Sb-PCF are 762 and 538 mA h g^{-1}, respectively. Due to the polarization, the discharge voltage drops and the specific capacity decays to 512 mA h g^{-1} in the 500th cycle. A discharge plateau is observed within the range 0.64–0.83 V during the first discharge. This, together with the capacity loss during the first cycle, is presumably due to the typical irreversible SEI formation.[14,25a] In the second and third cycles, Sb-PCF reversibly delivers a capacity of around 526 mA h g^{-1} for both cycles with a Coulombic efficiency of 97.7 %. The sodium storage capability of the Sb particles in the composite at current density of 0.5 A g^{-1} was calculated by deducting the capacity contributions from the nitrogen-doped porous carbon fiber ($\approx$350 mA h g^{-1}). The particles in the Sb-PCF electrode reach a reversible sodium storage capacity of 638 mA h g^{-1}, corresponding to 96.6% of the theoretical capacity of Sb (Na $\rightarrow$ Na$_3$Sb) and therefore an almost complete utilization of Sb. An overview over the rate capability examined at different specific currents ranging from 0.1 to 20 A g^{-1} (Figure 2C) is showing that the composite offers remarkable reversible capacities of 526, 501, 474, 435, 374, 311, and 186 mA h g^{-1} at current densities of 0.1, 1, 2, 5, 10, and 20 A g^{-1}, respectively, with similar shapes of the charge–discharge profiles and increasing voltage gaps. The voltage gaps are likely caused by remaining polarization and mechanical stress during the charge-discharge processes.[14,33] In comparison, the Sb-CF and CF electrodes only provide initial capacities of 352 and 190 mA h g^{-1} at 0.1 A g^{-1}, respectively (Supporting Information Figure S3A and B). Larger voltage gaps as compared to the Sb-PCF electrode are present for Sb-CF in the charge-discharge profiles at various current densities (Supporting Information Figure S3C). After 40 cycles at different current densities, the reversible capacity of Sb-PCF is still 527 mA h g^{-1} at 0.1 A g^{-1}, which is much higher than those of Sb-CF and CF (Figure 2D). When Sb-PCF was cycled at 0.5 A g^{-1}, a discharge capacity of 507 mA h g^{-1} can still be obtained after 500 cycles, corresponding to almost 97.5% of the initial capacity (Figure 2E). In comparison, Sb-CF only delivers a capacity of 236 mA h g^{-1} with a capacity retention of 71 % after 500 cycles. The results give evidence that Sb-PCF shows high rate capability and excellent cycling stability due to the small size of Sb and its surrounding nanopores in the carbon composite.

From a microscopic perspective, the morphological influence of Sb-PCF during operation can be understood as follows (Scheme 2A). During discharging, the Sb nanoparticles experience a volume expansion upon sodium
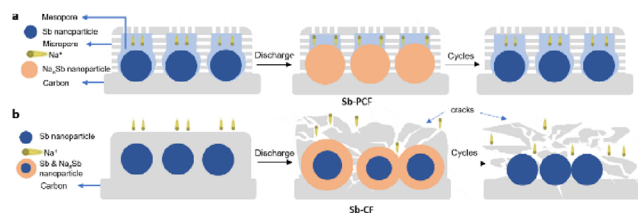
SCHEME 2 Suggested microstructural changes in the (A) Sb-PCF and (B) Sb-CF composites during operation

insertion. However, agglomeration of the particles can apparently be prevented. The mesoporous cages surrounded by micropores efficiently buffer the volumetric change of the encapsulated Sb nanoparticles during the charge-discharge processes and prevent their agglomeration. On the other hand, the micropores in the carbon fiber matrix do still offer sufficient pathways for the sodium ion transport, enabling the high rate capability despite the encapsulation of the sodium storing particles.[34] Nitrogen heteroatoms in the carbon material can further contribute to enhanced sodium transport.[35] In comparison, the Sb nanoparticles are wrapped by carbon without significant porosity in Sb-CF (Scheme 2B). In this composite, the Sb nanoparticles do not completely react, and irreversible processes become more pronounced. As a result, the Sb-CF composite shows comparably poor rate capability and cyclability.

To further verify the versatility of this preparation technique for other metal/carbon matrix composites, Sb nanoparticles were replaced by Sn nanoparticles and Sn-PCF was prepared through the same procedure. The TEM image of the as-synthesized SnO_2 nanoparticles confirms particle sizes in the range of 3–6 nm with a relatively narrow particle size distribution (Figure S1B, supporting information). XRD signals can be assigned to the tetragonal phase of SnO_2 (JCPDS No. 41–1445).[36] In comparison to Sb-PCF, the Sn-containing electrospun fibers have a slightly larger, but also uniform diameter of around 800 nm (Figure 3A). Elemental mapping (insets, Figure 3A) proves that the Sn nanoparticles are uniformly distributed in the nitrogen-doped carbon fibers. The SEM image reveals a rough surface topology with small pits, presumably being a result of the carbonization process and the inlaid Sn nanoparticles (Figure 3B). The Sn nanoparticles are uniformly embedded in the carbon matrix and the particle size remains around 5 nm (Figure 3C). The inset high-resolution TEM image shows lattice fringes of 0.278 nm, corresponding to the d-spacing of the (101) plane of tetragonal Sn. XRD analysis of the Sn-PCF composite is showing a diffraction pattern that can be indexed according to tetragonal Sn (JCPDS No. 4–673)[37] (Supporting Information Figure S1D). To quantify the Sn content in the Sn-PCF composite, TGA was carried out (Figure 3D). Based
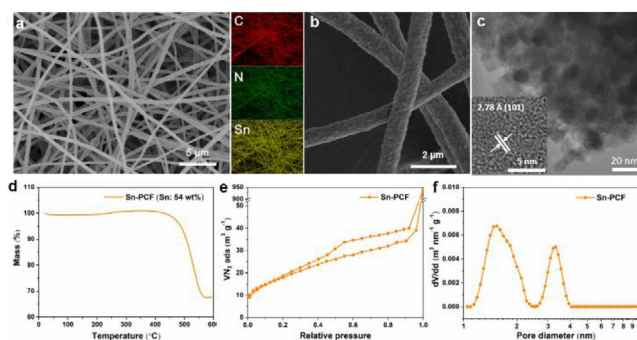

FIGURE 3 (A, B) SEM images of Sn-PCF at different magnifications. The inset in (A) shows the corresponding elemental mapping SEM-EDX (C, N and Sn); (C) TEM and HRTEM images (inset) of Sn-PCF; (D) TGA of Sn-PCF in air; (E) nitrogen physisorption (at −196°C) isotherms with (F) corresponding QSDFT pore size distribution of Sn-PCF
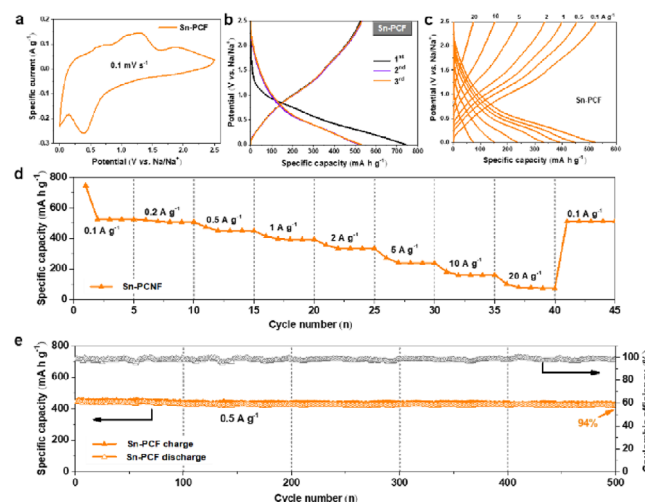

FIGURE 4 (A) CV curves of the Sn-PCF between 0–2.5 V at a scanning rate of 0.1 mV s^{-1}; (B) galvanostatic charge-discharge profiles of Sn-PCF for the first three cycles at a current density of 0.1 A g^{-1}; (C) galvanostatic charge-discharge profiles and (D) rate performance of the Sn-PCF cycled at various current densities from 0.1 A g^{-1} to 20 A g^{-1}; (E) cycling performance of the Sn–PCF at a cycling rate of 0.5 A g^{-1}

on a pronounced weight loss resulting from the oxidation of carbon, the total Sn content in the composite was calculated to be 54 wt% assuming SnO_2 as the oxidation product. Nitrogen physisorption measurements (Figure 3E) show that Sn-PCF exhibits a type IV-isotherm with a continuous slope above a relative pressure of 0.2 and a narrow hysteresis loop in the relative pressure range between 0.4 and 0.9.[27b] The pore size distribution (Figure 3F) shows that micropores and mesopores with sizes ranging from 1.3 to 4 nm are present. The surface area and the TPV of the composite were determined to be 54 m^2 g^{-1} and 0.06 cm^3 g^{-1}, respectively, indicating the

6 of 8 | **Electrochemical Science Advances** | Full article
doi.org/10.1002/elsa.202100010

Chemistry
Europe
European Chemical
Societies Publishing

micro/mesoporous structure of Sn-PCF (Table S1, supporting information).

In the CV curve of the Sn-PCF composite (Figure 4A), four weak peaks at 0.24, 0.58, 0.72 V and 1.05 V can be observed during the oxidation scan, which can be attributed to the desodation of $Na_{15}Sn_4$, Na_9Sn_4, NaSn, and $NaSn_5$, respectively.[18,38] The two reduction peaks at 0.38 V and 0 V can be assigned to the formation of the corresponding four Na_xSn alloys[38,39] and the storage of sodium into the expanded graphitic areas in the carbon fibers.[18] The first three galvanostatic charge–discharge profiles of the Sn-PCF electrode at a current density of 0.1 A g^{-1} reveal that the specific capacities after the first sodiation and desodiation are 739 and 523 mA h g^{-1}, respectively (Figure 4B). During the second and third cycles, the discharge and charge profiles overlapped, implying a good reversibility of the Sn-PCF electrode. In addition, the Sn-PCF shows a high rate performance (Figure 4C and D). Reversible capacities of 524, 507, 450, 393, 334, 239, 160, and 75 mA h g^{-1} can be retained at current densities of 0.1, 1, 2, 5, 10, and 20 A g^{-1}, respectively. To investigate the cyclability, Sn-PCF was cycled at a fixed current density of 0.5 A g^{-1}. The composite exhibits a high reversible capacity of 428 mA h g^{-1} over 500 cycles with 94% capacity retention (Figure 4E). Pulverization of the electrodes is a major problem of metallic anodes undergoing extensive volume changes during operation. To reveal possible reasons behind the remarkable stability of Sb- and Sn-PCF, the macroscopic appearance and the microstructure of the electrodes were investigated after 500 cycles. Digital photographs and the corresponding SEM images (Supporting Information Figure S4A and B) show that the electrodes preserve their freestanding form without pulverization. The fibrous morphology is fully maintained as well, indicating the outstanding structural stability of the material during battery cycling.

3 | CONCLUSION

Porous carbon fibers containing Sb or Sn nanoparticles were prepared by an electrospinning process followed by carbothermal reduction. Both composites offer a unique porous architecture that makes them promising for battery applications. The mesopores host the Sb and Sn nanoparticles, which are just a few nm in size, while the microporosity provides the pathways for efficient ion transport. Together with the fibrous morphology, the porosity helps to efficiently balance the mechanical stress induced by volume expansion/contraction, prevent pulverization and agglomeration of the Sb and Sn nanoparticles and enhance the ion transport. As anode materials for SIBs, the Sb-PCF and Sn-PCF composites offer remarkable cycling performance with capacities of 507 mA h g^{-1} and 428 mA h g^{-1}

after 500 cycles at 0.5 A g^{-1}, respectively. Even at a high current density of 20 A g^{-1}, capacities of 197 and 75 mA h g^{-1} can be achieved by Sb-PCF and Sn-PCF, respectively. Our work shows that the encapsulation of nanoparticles in porous carbon fibers could be a promising strategy to make even materials with such extensive volume change useful for battery applications. As many electrochemically interesting materials are available in the form of nanoparticles, it can be expected that the proposed method can be generally applied beyond the two examples Sb and Sn presented here.

4 | EXPERIMENTAL SECTION

4.1 | Synthesis of Sb_2O_3 nanoparticles

1 mmol $Sb(CH_3CO_2)_3$ ($\geq$ 97 %, Alfa Aesar) was dissolved slowly in 3 mL benzylamine (99.0 %, Fluka). After vigorous stirring at room temperature for 2 min, 2 mL oleylamine ($\geq$ 96 %, Acros) was added dropwise and the mixture was stirred for 30 min. A white precipitate formed, which was collected by centrifugation and washed with ethanol for 3 times. Finally, the precipitate was dried in vacuum at 80°C overnight for later use.

4.2 | Synthesis of SnO_2 nanoparticles

The SnO_2 nanoparticles were prepared by a modified microwave-assisted method adapted from a previous report.[21] In a typical procedure, 0.8 mL $SnCl_4$ (99.99 %, ABCR), 15 mL benzyl alcohol ($\geq$99%, Sigma-Aldrich), and 5 mL toluene were mixed in a 35 ml microwave glass vial. After vigorous stirring for 30 min at room temperature, the mixture was heated by a microwave reactor (CEM Hybrid) at 155°C for 30 min with high stirring rate. The precipitate was separated from the liquid phase by centrifugation, washed at least 3 times by ethanol, and finally dried in a vacuum overnight at 80 °C.

4.3 | Synthesis of Sb/Sn-PCFs

Sb/Sn-PCFs were synthesized through electrospinning followed by carbothermal reduction at high temperature. 200 mg Sb_2O_3 or SnO_2 nanoparticles were dispersed in 1.8 g *N,N*-dimethylformamide (DMF) (anhydrous, 99.8%, Sigma–Aldrich), followed by addition of 200 mg polyacrylonitrile (PAN) (average Mw 150,000, Sigma–Aldrich) under stirring at 60 °C for 12 h. The electrospinning precursor was loaded to a 2 mL syringe and mounted on a syringe pump in a spinning machine (Professional Electrospinner, Yflow, Spain). A positive high voltage was connected via an alligator clip to the needle with an inner diameter of

7 of 8   **Electrochemical Science Advances**   Full article
doi.org/10.1002/elsa.202100010

**Chemistry
Europe**
European Chemical
Societies Publishing

0.5 mm and outer diameter of 1 mm. A grounded rotating drum covered with aluminum foil was employed to collect the fibers at a rotation speed of 200 rpm for a duration of 25 min. Process parameters were fixed at a high voltage of +13 kV, flow rate of 2 mL h^{-1} and distance from tip to the collector of 15 cm. The temperature was 23 °C and the humidity 40−50%. Subsequently, the Sb$_2$O$_3$/SnO$_2$-PAN fibers were pre-oxidized at 250°C under air for 30 min, followed by carbonization and carbothermal reduction in a chamber furnace at 600°C (for Sb-PCF) or 700°C (for Sn-PCF) for 2 h under N$_2$ gas flow with a heating rate of 2°C/min.

4.4 | Synthesis of Sb-CF

Sb-CF was synthesized according to a reported procedure with slight modifications.[22] The electrospinning precursor was prepared by dissolution of 600 mg SbCl$_3$ and 400 mg PAN in 3 g DMF by stirring at room temperature for 2 h. The process of electrospinning and the subsequent pre-oxidation was the same as that of Sb-PCF. Finally, the fibers were carbonized in a tube furnace at 600°C for 2 h under a H$_2$ (5 vol %) / Ar (95 vol %) atmosphere with a heating rate of 2°C/min to obtain the Sb-CF sample.

4.5 | Material characterization

Nitrogen physisorption experiments were carried out at −196°C on a Quadrasorb apparatus (40–60 mg sample) from Quantachrome Instruments. Prior to all measurements, the samples were outgassed at 150°C for 20 h under vacuum. Total pore volumes (TPV) were determined at $P/P_0 = 0.95$. Specific surface area (SSA) and pore size distributions were calculated using the quenched-solid density functional theory (QSDFT) method (adsorption branch kernel) for N$_2$ adsorbed on carbon with a slit/cylindrical pore shape at −196°C. Further structural characterization was carried out by scanning electron microscopy (SEM, LEO 1550-Gemini) operating at 3 kV and transmission electron microscopy (TEM, EM 912 Omega/Carl-Zeiss Oberkochen, Hitachi HT7700 microscope, and X-FEG FEI Talos). To prepare the TEM samples, the composites were dispersed in ethanol by sonication for 10 min, followed by dropping several droplets of the dispersion on a carbon-coated copper TEM grid and drying at room temperature. Thermogravimetric analysis (TGA) was conducted with a Netzsch TG 209 F1 device under a constant artificial air (80 % N$_2$ and 20 % O$_2$) flow in platinum pans at a heating rate of 5°C/min to 1000°C. X-ray powder diffraction (XRD) measurements were performed on a PANalytical Empyrean diffractometer equipped with a Cu Kα X-ray tube (45 kV, 40 mA).

4.6 | Electrochemical measurements

The free-standing Sb/Sn-PCF, Sb-CF, and CF samples were punched into free-standing disks of 10 mm in diameter, which were directly used as working electrodes. The areal loading of an electrode was about 0.5 mg cm^{-2}. The half-cell tests were carried out using Swagelok-type cells assembled in an argon-filled glove box (H$_2$O < 0.1 ppm, O$_2$ < 0.1 ppm). Sodium metal (11 mm in diameter) was used as both counter and reference electrodes. Glass fibers (Whatman GF/C, 13 mm in diameter) were employed as the separators. The electrolyte was 1 M NaClO$_4$ in ethylene carbonate/propylene carbonate/fluoroethylene carbonate (45:45:10 by mass). The Swagelok cell was assembled using the working and counter electrodes sandwiching the separator, with 500 μL electrolyte and a copper foil as the current collector for the working electrode. Biologic MPG-2 galvanostat/potentiostat and Biologic instrument (BCS series) were used for electrochemical characterization. All measurements were performed at room temperature. Cyclic voltammetry (CV) tests were performed at scan rates of 0.1 mV s^{-1}. Galvanostatic charge/discharge with potential limitation (GCPL) was applied at specific currents between 0.1 and 20 A g^{-1} in a voltage range from 0 V to 2.5 V. The specific capacity, Q (mA h g^{-1}), was calculated according to the following equation:

$$Q = \frac{Q_{dis}}{m} \tag{1}$$

where Q_{dis} (mA h) is the charge of the discharging cycle, and m (g) is the mass of a single electrode.

DATA AVAILABILITY STATEMENT
Data available on request from the authors.

REFERENCES
1. a) N. A. Kaskhedikar, J. Maier, *Adv. Mater.* **2009**, *21*, 2664–2680; b) L. W. Ji, Z. Lin, M. Alcoutlabi, X. W. Zhang, *Energy Environ. Sci.* **2011**, *4*, 2682–2699.
2. G. Zubi, R. Dufo-Lopez, M. Carvalho, G. Pasaoglu, *Renew. Sust. Energ. Rev.* **2018**, *89*, 292–308.

3. a) M. S. Balogun, Y. Luo, W. T. Qiu, P. Liu, Y. X. Tong, *Carbon* **2016**, *98*, 162–178; b) C. Nithya, S. Gopukumar, *WIREs Energy Environ.* **2015**, *4*, 253–278.

4. a) L. Wei, K. Tian, X. Y. Zhang, Y. Y. Jin, T. Shi, X. Guo, *ACS Sustainable Chem. Eng.* **2016**, *4*, 6463–6472; b) R. S. Kalubarme, J. Y. Lee, C. J. Park, *ACS Appl. Mater. Interfaces* **2015**, *7*, 17226–17237.

5. a) Y. Sun, L. Zhao, H. L. Pan, X. Lu, L. Gu, Y. S. Hu, H. Li, M. Armand, Y. Ikuhara, L. Q. Chen, X. J. Huang, *Nat. Commun.* **2013**, *4*, 1–10; b) Y. Xiao, S. H. Lee, Y. K. Sun, *Adv. Energy Mater.* **2017**, *7*, 1601329.

6. a) P. R. Abel, M. G. Fields, A. Heller, C. B. Mullins, *ACS Appl. Mater. Interfaces* **2014**, *6*, 15860–15867; b) L. Y. Liang, Y. Xu, C. L. Wang, L. Y. Wen, Y. G. Fang, Y. Mi, M. Zhou, H. P. Zhao, Y. Lei, *Energy Environ. Sci.* **2015**, *8*, 2954–2962.

7. a) C. Chen, K. Fu, Y. Lu, J. D. Zhu, L. G. Xue, Y. Hu, X. W. Zhang, *RSC Adv.* **2015**, *5*, 30793–30800; b) H. L. Zhu, Z. Jia, Y. C. Chen, N. Weadock, J. Y. Wan, O. Vaaland, X. G. Han, T. Li, L. B. Hu, *Nano Lett.* **2013**, *13*, 3093–3100.

8. a) L. F. Xiao, Y. L. Cao, J. Xiao, W. Wang, L. Kovarik, Z. M. Nie, J. Liu, *Chem. Commun.* **2012**, *48*, 3321–3323; b) H. S. Hou, M. J. Jing, Y. C. Yang, Y. R. Zhu, L. B. Fang, W. X. Song, C. C. Pan, X. M. Yang, X. B. Ji, *ACS Appl. Mater. Interfaces* **2014**, *6*, 16189–16196.

9. a) J. W. Wang, X. H. Liu, S. X. Mao, J. Y. Huang, *Nano Lett.* **2012**, *12*, 5897–5902; b) P. K. Dutta, U. K. Sen, S. Mitra, *RSC Adv.* **2014**, *4*, 43155–43159.

10. a) H. J. Ying, W. Q. Han, *Adv. Sci.* **2017**, *4*, 1700298; b) M. Zhang, T. Wang, G. Cao, *Int. Mater. Rev.* **2015**, *60*, 330–352.

11. X. L. Wang, M. Feygenson, M. C. Aronson, W. Q. Han, *J. Phys. Chem. C* **2010**, *114*, 14697–14703.

12. P. G. Bruce, B. Scrosati, J. M. Tarascon, *Angew. Chem., Int. Ed.* **2008**, *47*, 2930–2946.

13. a) R. Y. Yan, K. Leus, J. P. Hofmann, M. Antonietti, M. Oschatz, *Nano Energy* **2020**, *67*, 104240; b) C. C. Chen, J. Maier, *Nat. Energy* **2018**, *3*, 102–108.

14. J. Duan, W. Zhang, C. Wu, Q. J. Fan, W. X. Zhang, X. L. Hu, Y. H. Huang, *Nano Energy* **2015**, *16*, 479–487.

15. L. Pan, H. J. Huang, M. Zhong, M. Niederberger, *Energy Storage Mater.* **2019**, *16*, 519–526.

16. L. W. Ji, Z. K. Tan, T. Kuykendall, E. J. An, Y. B. Fu, V. Battaglia, Y. G. Zhang, *Energy Environ. Sci.* **2011**, *4*, 3611–3616.

17. R. Y. Yan, E. Josef, H. J. Huang, K. Leus, M. Niederberger, J. P. Hofmann, R. Walczak, M. Antonietti, M. Oschtz, *Adv. Funct. Mater.* **2019**, *29*, 1902858.

18. M. Sha, H. Zhang, Y. T. Nie, K. Q. Nie, X. X. Lv, N. Sun, X. K. Xie, Y. Y. Ma, X. H. Sun, *J. Mater. Chem. A* **2017**, *5*, 6277–6283.

19. K. Shiva, H. B. Rajendra, A. J. Bhattacharyya, *ChemPlusChem* **2015**, *80*, 516–521.

20. H. S. Hou, C. E. Banks, M. J. Jing, Y. Zhang, X. B. Ji, *Adv. Mater.* **2015**, *27*, 7861–7866.

21. J. H. Ba, J. Polleux, M. Antonietti, M. Niederberger, *Adv. Mater.* **2005**, *17*, 2509–2512.

22. Y. J. Zhu, X. G. Han, Y. H. Xu, Y. H. Liu, S. Y. Zheng, K. Xu, L. B. Hu, C. S. Wang, *ACS Nano* **2013**, *7*, 6378–6386.

23. H. L. Zhao, D. H. L. Ng, Z. Q. Lu, N. G. Ma, *J. Alloys Compd.* **2005**, *395*, 192–200.

24. a) D. B. Wang, Y. H. Zhou, C. X. Song, M. Q. Shao, *J. Cryst. Growth* **2009**, *311*, 3948–3953; b) T. Cebriano, B. Mendez, J. Piqueras, *Mater. Chem. Phys.* **2012**, *135*, 1096–1103.

25. a) L. Wu, X. H. Hu, J. F. Qian, F. Pei, F. Y. Wu, R. J. Mao, X. P. Ai, H. X. Yang, Y. L. Cao, *Energy Environ. Sci.* **2014**, *7*, 323–328; b) W. Luo, S. Lorger, B. Wang, C. Bommier, X. L. Ji, *ChemComm* **2014**, *50*, 5435–5437.

26. Y. N. Ko, Y. C. Kang, *ChemComm* **2014**, *50*, 12322–12324.

27. a) S. J. Kim, S. Lee, S. H. Hong, *Appl. Spectrosc. Rev.* **2016**, *51*, 636–645; b) R. Y. Yan, T. Heil, V. Presser, R. Walczak, M. Antonietti, M. Oschatz, *Adv. Sustain. Syst.* **2018**, *2*, 1700128; c) M. Rose, Y. Korenblit, E. Kockrick, L. Borchardt, M. Oschatz, S. Kaskel, G. Yushin, *Small* **2011**, *7*, 1108–1117.

28. a) H. G. Wang, Z. Wu, F. L. Meng, D. L. Ma, X. L. Huang, L. M. Wang, X. B. Zhang, *ChemSusChem* **2013**, *6*, 56–60; b) Y. L. Cao, L. F. Xiao, M. L. Sushko, W. Wang, B. Schwenzer, J. Xiao, Z. M. Nie, L. V. Saraf, Z. G. Yang, J. Liu, *Nano Lett.* **2012**, *12*, 3783–3787; c) Z. M. Liu, X. Y. Yu, X. W. D. Lou, U. Paik, *Energy Environ. Sci.* **2016**, *9*, 2314–2318; d) Y. Z. Zhang, L. Chen, Y. Meng, J. Xie, Y. Guo, D. Xiao, *J. Power Sources* **2016**, *335*, 20–30.

29. N. Zhang, Y. C. Liu, Y. Y. Lu, X. P. Han, F. Y. Cheng, J. Chen, *Nano Res.* **2015**, *8*, 3384–3393.

30. J. D. Zhu, C. Chen, Y. Lu, Y. Q. Ge, H. Jiang, K. Fu, X. W. Zhang, *Carbon* **2015**, *94*, 189–195.

31. L. Baggetto, P. Ganesh, C. N. Sun, R. A. Meisner, T. A. Zawodzinski, G. M. Veith, *J. Mater. Chem. A* **2013**, *1*, 7985–7994.

32. T. Q. Chen, Y. Liu, L. K. Pan, T. Lu, Y. F. Yao, Z. Sun, D. H. C. Chua, Q. Chen, *J. Mater. Chem. A* **2014**, *2*, 4117–4121.

33. V. A. Sethuraman, V. Srinivasan, A. F. Bower, P. R. Guduru, *J. Electrochem. Soc.* **2010**, *157*, A1253–A1261.

34. W. H. Li, S. H. Hu, X. Y. Luo, Z. L. Li, X. Z. Sun, M. S. Li, F. F. Liu, Y. Yu, *Adv. Mater.* **2017**, *29*, 1605820.

35. L. Chen, R. Y. Yan, M. Oschatz, L. Jiang, M. Antonietti, K. Xiao, *Angew. Chem., Int. Ed.* **2020**, *59*, 9067–9073.

36. F. Gu, S. F. Wang, C. F. Song, M. K. Lu, Y. X. Qi, G. J. Zhou, D. Xu, D. R. Yuan, *Chem. Phys. Lett.* **2003**, *372*, 451–454.

37. Y. Li, J. W. Shi, Y. Liang, *Int. J. Electrochem. Sci.* **2018**, *13*, 2366–2378.

38. H. J. Ying, S. L. Zhang, Z. Meng, Z. X. Sun, W. Q. Han, *J. Mater. Chem. A* **2017**, *5*, 8334–8342.

39. Y. C. Liu, N. Zhang, L. F. Jiao, J. Chen, *Adv. Mater.* **2015**, *27*, 6702–6707.

SUPPORTING INFORMATION

Additional supporting information may be found online in the Supporting Information section at the end of the article.